nature energy

ARTICLES

PUBLISHED: 18 JULY 2016 | ARTICLE NUMBER: 16102 | DOI: 10.1038/NENERGY.2016.102

A redox-flow battery with an alloxazine-based organic electrolyte

Kaixiang Lin[1], Rafael Gómez-Bombarelli[1], Eugene S. Beh[1,2], Liuchuan Tong[1], Qing Chen[2], Alvaro Valle[3], Alán Aspuru-Guzik[1], Michael J. Aziz[2]* and Roy G. Gordon[1,2]*

Redox-flow batteries (RFBs) can store large amounts of electrical energy from variable sources, such as solar and wind. Recently, redox-active organic molecules in aqueous RFBs have drawn substantial attention due to their rapid kinetics and low membrane crossover rates. Drawing inspiration from nature, here we report a high-performance aqueous RFB utilizing an organic redox compound, alloxazine, which is a tautomer of the isoalloxazine backbone of vitamin B_2. It can be synthesized in high yield at room temperature by single-step coupling of inexpensive *o*-phenylenediamine derivatives and alloxan. The highly alkaline-soluble alloxazine 7/8-carboxylic acid produces a RFB exhibiting open-circuit voltage approaching 1.2 V and current efficiency and capacity retention exceeding 99.7% and 99.98% per cycle, respectively. Theoretical studies indicate that structural modification of alloxazine with electron-donating groups should allow further increases in battery voltage. As an aza-aromatic molecule that undergoes reversible redox cycling in aqueous electrolyte, alloxazine represents a class of radical-free redox-active organics for use in large-scale energy storage.

Improved methods for storing electrical energy from intermittent renewable sources are needed to support the rapid deployment of photovoltaic and wind power[1–3]. A promising approach for safe and cost-effective stationary energy storage uses redox-flow batteries (RFBs), in which the energy is stored in fluids held outside the power conversion electrochemical cell[4,5]. This permits the independent engineering of energy (electrolyte volume and/or concentration) and power (cell area) capacities and enables the attainment of the high energy-to-power ratios (that is, long discharge durations at rated power) necessary to deliver energy from photovoltaics and wind when it is needed. Since the invention of RFBs in the 1970s, the development efforts for their electrolyte materials—the core component of RFBs—have concentrated on single metal ions such as vanadium, iron and chromium, where the battery voltages are fixed by the reduction potentials of these ions, and their solubilities and stabilities are governed by the pH and composition of the supporting electrolyte[6,7]. However, their development has been impeded by one or more shortcomings such as high electrolyte corrosivity, toxicity, cost, membrane crossover rate, or sluggish reaction kinetics.

Contrary to the limited number of metal ions suitable for RFBs, organic molecules display high chemical diversity, allowing optimization of electrolyte properties such as higher solubility (by adding solubilizing groups), higher voltage (by varying the electron-donating properties of functional groups), and lower membrane crossover rate (by tuning the molecular size or net charge on the molecules). Recently, researchers have demonstrated RFBs of much improved performance by rational design of organic-based electrolyte materials (summarized in Table 1)[8–13]. For instance, ref. 8 utilized a sulfonic acid-functionalized 9,10-anthraquinone, which showed fast kinetics and high solubility in a supporting electrolyte of sulfuric acid; by pairing it up with cheap bromine/hydrobromic acid, the team showed approximately a threefold reduction of the potential cost of electrolyte materials, compared with state-of-art all-vanadium RFBs[8,9]. The toxicity and corrosivity of bromine, however, limit its use to industrial and utility settings. By switching from acidic to alkaline supporting electrolyte, ref. 10 demonstrated a less corrosive and non-toxic RFB using hydroxylated 9,10-anthraquinone and a food additive, ferrocyanide, targeted for residential and commercial usage. To reduce membrane cost while maintaining a low membrane crossover rate, ref. 11 prepared polymeric methyl viologen and (2,2,6,6-tetramethylpiperidin-1-yl)oxidanyl (TEMPO) that showed almost no sign of membrane crossover when cheap dialysis membranes were used in place of expensive cation-exchange membranes. Despite these great advances, each system still has potential for further improvement, such as replacing toxic halogen species with high-performance organic molecules, increasing the ion conductivity and energy density of alkaline systems, and reducing the high electrolyte viscosity associated with the dissolution of polymers at practical concentrations. To accelerate the development of organic-based RFBs, more compounds with useful redox potential, high solubility, and ease of synthesis are highly desired. Previous aqueous organic-based RFBs have utilized only three types of stable redox-active species: quinones, TEMPO and methyl viologen, as shown in Table 1. To date, tailored improvements have been proved to be possible only in quinone systems. An aza-aromatic compound, quinoxaline, has also been identified as a potential electrolyte for flow batteries[14], but its capacity fades rapidly during cycling of a full cell[15].

Gaining inspiration from naturally occurring flavin cofactors, here we report a novel alloxazine-based aqueous organic RFB. Alloxazines can be synthesized via a simple and high-yielding coupling reaction between *o*-phenylenediamine derivatives and alloxan in acetic acid and boric acid at room temperature and atmospheric pressure (Table 2)[16–18]. Functionalization of alloxazine

[1]Department of Chemistry and Chemical Biology, Harvard University, 12 Oxford Street, Cambridge, Massachusetts 02138, USA. [2]Harvard John A. Paulson School of Engineering and Applied Sciences, 29 Oxford Street, Cambridge, Massachusetts 02138, USA. [3]Harvard College, Cambridge, Massachusetts 02138, USA. *e-mail: maziz@harvard.edu; gordon@chemistry.harvard.edu

Table 1 | High-performance organic-based aqueous redox-flow batteries.

Positive electrolyte	Negative electrolyte	No. of cycles (condition)	Capacity retention per cycle (%)*	Energy density ($Wh\,l^{-1}$)	Voltage (V)	Year of publication	Merit (limitation)
Bromine/hydrobromic acid	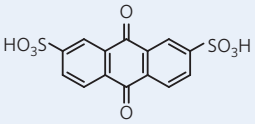 Anthraquinone-2,7-disulfonic acid	10	99	16	0.86	2014[8]	Low cost and high performance (toxic bromine)
		750	99.84	16	0.86	2014[9]	
Ferrocyanide/ferricyanide	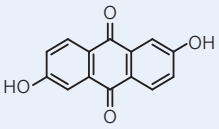 2,6-dihydroxy-anthraquinone	100	99.1	6.8	1.2	2015[10]	Non-toxic and less corrosive electrolyte (reduced ion conductivity w.r.t. proton)
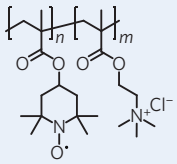 TEMPO polymer	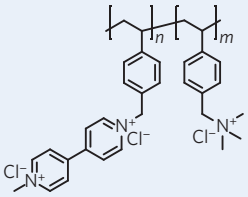 Viologen polymer	100	~99.75†	10	1.15	2015[11]	Cheap dialysis membrane (high electrolyte viscosity)
		10,000 (non-flow cell)	>99.99	10	1.15	2015[11]	
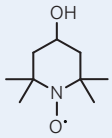 4-hydroxy-TEMPO	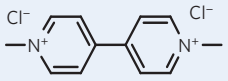 Methyl viologen	100 (low conc.)	>99.99	8.4	1.25	2015[13]	Low cost all-organic electrolyte (low current density)
		100 (high conc.)	99.89	8.4	1.25	2015[13]	

This table focuses primarily on comparing molecular structures of redox-active organic molecules and evaluating their electrochemical stability on the basis of capacity retention. *Capacity retention per cycle was derived from total capacity retention divided by total number of charge–discharge cycles. †The capacity retention value was estimated on the basis of the capacity retention versus cycle number graph in Fig. 4 from ref. 11.

with a carboxylic acid group renders the alloxazine molecule highly soluble in alkaline solution—up to 2 M in pH 14 KOH, which corresponds to a charge density of $108\,Ah\,l^{-1}$. By pairing it up with ferri/ferrocyanide as the positive electrolyte, we built a high-performance RFB characterized by an open-circuit voltage approaching 1.2 V, with current efficiency and capacity retention exceeding 99.7% and 99.98% per cycle, respectively. Enabled by a high-throughput computational study, a relationship between different alloxazine functional groups and their effects on reduction potential was established and exploited to guide the design of future alloxazine-based electrolyte materials. For instance, by replacing the carboxylic acid group with another alkaline-soluble hydroxyl group, the battery voltage can be further raised by almost 10%.

Rational design of electrolyte material

Designing an appropriate organic molecule as electrolyte material starts from identifying redox-active cores followed by functionalization of the core structure to achieve a practical reduction potential and solubility. We observed that riboflavin 5′ phosphate (FMN), a highly water-soluble compound derived from vitamin B_2, undergoes two-electron reduction via a flavin semiquinone radical intermediate on its isoalloxazine backbone (Supplementary Fig. 1)[19,20]. In alkaline solution, it exhibited high reversibility and a low reduction potential of −0.53 V versus SHE (Fig. 1a). Further exploration of its isoalloxazine motif led to the discovery that lumichrome, an alloxazine derivative that differs from isoalloxazine by its diazabutadiene double bond configuration, exhibited a much lower reduction potential of −0.70 V versus SHE (Fig. 1b). Alloxazine had previously been studied in the solid state as an anode material for non-aqueous lithium and sodium ion batteries[21]. However, the low solubility of alloxazine in a wide range of solvents presents a challenge for solution-phase applications. To increase its solubility in aqueous solution, we functionalized the alloxazine core with an alkaline-soluble carboxylic acid group by coupling *o*-phenylenediamine-4-carboxylic acid (also known as 3,4-diaminobenzoic acid) with alloxan to afford an isomeric mixture of alloxazine 7/8-carboxylic acid (ACA) in almost 100% yield (Supplementary Fig. 2). The reduction potential of ACA as measured by cyclic voltammetry is −0.62 V versus SHE (Fig. 1c). The larger separation between its oxidation and reduction peaks than those of FMN and lumichrome is likely to be due to slower kinetics. From our rotating-disc electrode measurement, the reduction rate constant was measured to be $1.2 \pm 0.2 \times 10^{-5}\,cm\,s^{-1}$ (Supplementary Fig. 3). Nevertheless, this value is still an order of magnitude higher than that of the slower side of all-vanadium RFBs[6].

Besides the large shift in reduction potential moving from isoalloxazine to alloxazine, we also observed a significant increase in chemical stability in alkaline conditions. Whereas cyclic voltammetry measurement of 0.5 M FMN in an alkaline solution revealed an almost 70% decrease in reduction signal within 2 weeks,

Table 2 | Reaction scheme and summary of alloxazine synthesis from the literature.

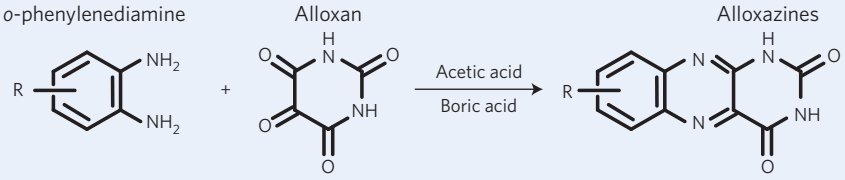

o-phenylenediamine	Alloxazines	Reaction time (h)	Yield (%)	Reference
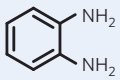	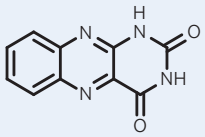 Alloxazine	2	87	Ref. 16
		2	95	Ref. 17
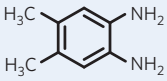	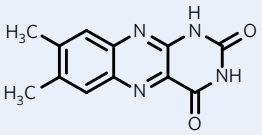 Lumichrome	2	95	Ref. 16
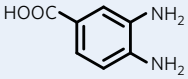	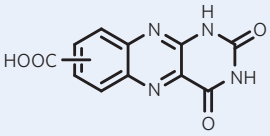 Alloxazine7/8-carboxylic acid (ACA)	3	100	Ref. 18
		3	95	This work
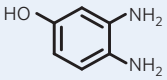	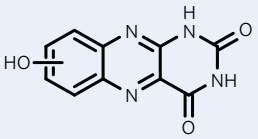 7/8-hydroxyalloxazine	3	86	This work
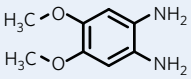	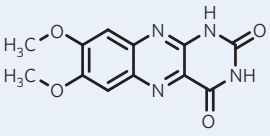 7,8-dimethoxyalloxazine	2	89	Ref. 16
		2	94	This work

Alloxazines with different functional groups (-R) can be prepared by coupling o-phenylenediamine derivatives with alloxan in the presence of acetic acid and boric acid.

an ACA solution at the same concentration showed almost no sign of degradation (Supplementary Fig. 4). Quantification of ACA stability was achieved by proton nuclear magnetic resonance (^{1}H NMR) analysis of a 0.5 M solution of ACA maintained at pH 14 over the course of six weeks. The decomposition of ACA, assuming first-order kinetics (R^2 = 0.991), had a rate constant of 1.39×10^{-3} d^{-1}, equivalent to a solution half-life of 500 days (Supplementary Fig. 5). This combination of lower reduction potential (−0.62 V versus −0.53 V) and higher chemical stability (500 days versus 10 days half-life for FMN at pH 14) makes ACA a much better candidate for an electrolyte material.

Electrochemical full-cell study

To demonstrate ACA in a full cell, we paired ACA with ferri/ferrocyanide (Fig. 1c,d). The battery was assembled using 0.5 M ACA (1.5 mmol) as the negative electrolyte and 0.4 M ferrocyanide (4.5 mmol) + 40 mM ferricyanide (0.46 mmol) as the positive electrolyte. Both solutions were adjusted to pH 14 by KOH. Excess quantities of ferrocyanide and ferricyanide were used to ensure that the negative terminal remained the capacity-limiting side for the purpose of evaluating its electrochemical stability during cycling. The resulting alkaline aqueous RFB showed an open-circuit voltage (OCV) approaching 1.2 V. The OCV versus state of charge (SOC) monotonically increased from 10% to 90% SOC (Fig. 2a). Polarization studies conducted at room temperature showed a peak power density of 0.35 W cm^{-2} at a current density of 0.58 A cm^{-2}. The linearity of the polarization curves allows us to derive a polarization area-specific resistance, which is 1.03 Ω cm^2 at 50% SOC. About 70% of this cell area-specific resistance is contributed by the membrane (Supplementary Fig. 6), similar to our previous observation[10]. Note that ACA redox kinetics do not show up as a significant kinetic overvoltage loss (that is, a nonlinearity at the low-overvoltage region) in the polarization curve, probably owing to the large surface area provided by the porous carbon electrodes. The electrochemical stability of ACA was evaluated on the basis of an extended charge–discharge study over 400 cycles (Fig. 2c).

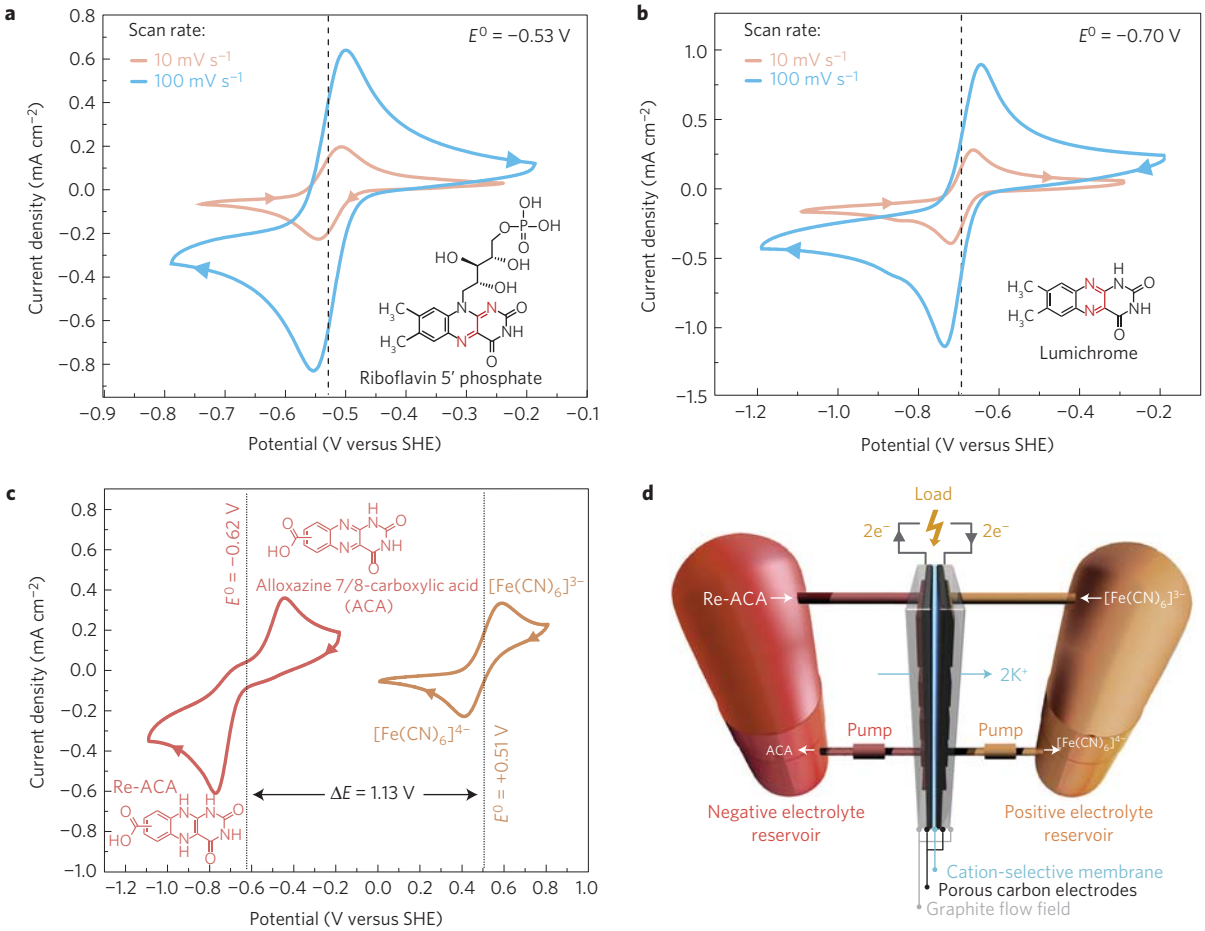

Figure 1 | Cyclic voltammogram and cell schematic. a,**b**, Molecular structures and cyclic voltammogram of 2 mM riboflavin 5′ phosphate (FMN) and lumichrome, respectively, scanned at 10 mV s^{-1} and 100 mV s^{-1} on a glassy carbon electrode. **c**, Cyclic voltammogram of 2 mM alloxazine 7/8-carboxylic acid (ACA) (red curve) and ferrocyanide (gold curve) scanned at 100 mV s^{-1} on a glassy carbon electrode; arrows indicate scan direction. **d**, Schematic of a cell in discharge mode. Grey arrows indicate flow direction of electrons and white arrows indicate electrolyte solution flow. The blue arrow indicates migration of cations across the membrane. Essential components of electrochemical cells are labelled with colour-coded lines and text.

The current efficiency exceeded 99.7% at 0.1 A cm^{-2}, which is indicative of negligible side reactions during cell cycling and a low crossover rate through the membrane. The round-trip energy efficiency in this cycling experiment averaged around 63%. The battery exhibited a remarkably high capacity retention rate of more than 91% over 400 cycles, or a capacity loss rate of 0.023% per cycle. To further analyse capacity retention, we compared the total charge from the cell before and after cycling using chronoamperometry to charge and discharge the cell at constant voltage (Supplementary Fig. 7). From this result, the measured capacity retention from 400 cycles was 95%, that is, the loss rate was 0.013% per cycle. We believe the discrepancy between this measurement and the capacity retention observed during constant-current cycling was due to an increase in system resistance (which we infer from decreasing energy efficiency with cycle number); this effect moved the charging and discharging curves closer to the cutoff voltages, resulting in less complete charging and discharging with increasing cycle count (Supplementary Fig. 8). We expect further cell development, including variations in pH, membrane and sealing method, to lead to a further improvement of capacity retention. By increasing the concentration of ACA to 1 M, we increased the electrolyte charge density by almost twofold (Supplementary Fig. 9a). Together with adjusted cell compression and higher ACA concentration, we were able to improve round-trip energy efficiency to 74%, while retaining the same level of current efficiency (99.7%) and capacity retention per cycle (99.95%) (Supplementary Fig. 9b).

Theoretical modelling and screening

One useful feature of organic electrolyte materials is the ability to optimize their properties through chemical modification, a process that can be accelerated by virtual testing with computational methods[8,22]. We assayed the chemical landscape around the alloxazine backbone by computing the properties of derivatives bearing one to four copies of each of seven functional groups. Selected examples of alloxazine derivatives subjected to the theoretical modelling are shown in Table 3 (a complete table of the rest of the studied alloxazine derivatives can be found in Supplementary Table 1).

Figure 3 shows the variation in predicted standard reduction potential (E^0) within the alloxazine class. The additive effect of electron-donating and electron-withdrawing groups is observed as they lower and raise the reduction potential, respectively, across a range of 400 mV. Hydroxyl, methyl and methoxy substituents afford the largest increases in cell potential. We prepared 7/8-hydroxyalloxazine and 7,8-dimethylalloxazine via the aforementioned *o*-phenylenediamine–alloxan coupling chemistry (Table 2 and Supplementary Figs 10 and 11). Cyclic voltammetry of these two compounds showed values below −0.73 V (~110 mV lower than ACA), potentially raising the battery voltage by another 10% (Fig. 3c,d).

In addition to tuning its reduction potential, modification of alloxazine with appropriate functional groups could also improve its chemical stability. Alloxazines undergo a ring-opening

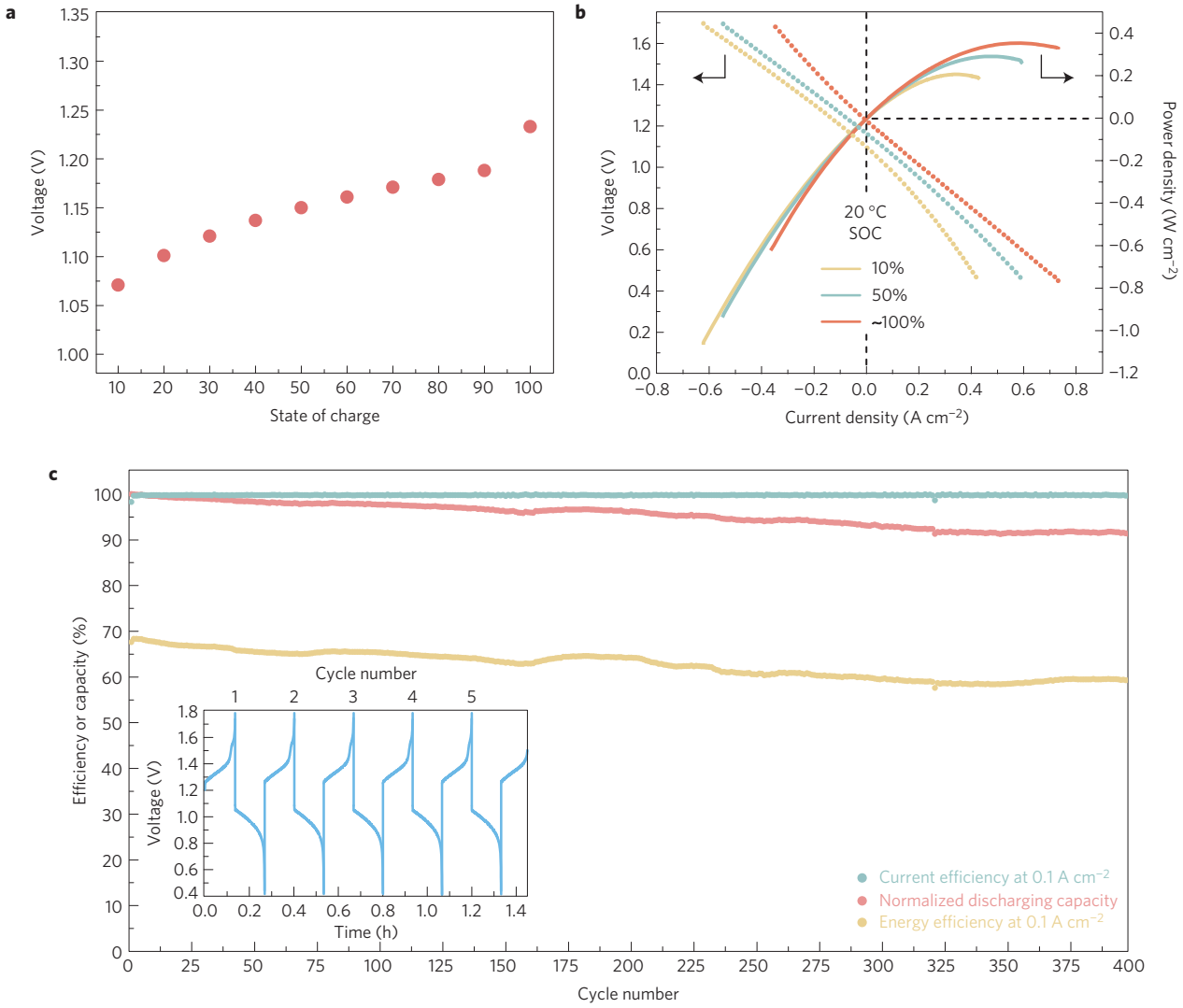

Figure 2 | Cell performance. a, Cell OCV versus SOC. All potentials were taken when the cell voltage stabilized to within ± 1 mV. SOC of 100% was reached by a potentiostatic hold at 1.5 V until the current decreased to below 5 mA cm^{-2}. **b**, Cell voltage and power density versus current density at 20 °C, at 10%, 50% and ~100% SOC. Electrolyte composition: 0.5 M ACA and 0.4 M ferrocyanide + 40 mM ferricyanide were used in negative electrolyte and positive electrolyte, respectively. **c**, Capacity retention, current efficiency and energy efficiency values over 400 cycles at 0.1 A cm^{-2}. The normalized discharging capacity is evaluated on the basis of the capacity of the first discharge cycle. (Inset: representative voltage versus time curves during 400 charge–discharge cycles at 0.1 A cm^{-2}, recorded between the first and fifth cycles.)

reaction in aqueous solvent via addition of water to the amidic carbonyls followed by continued hydrolysis to redox-inactive species (Supplementary Fig. 12)[23]. Increases in pH catalyse the hydrolysis process, as observed in the FMN stability study and informed by the literature[24,25]. Nevertheless, the low pK_a values at the amide nitrogen (8.4 and 11.4 for lumichrome[26]) result in the accumulation of two negative charges in the imidic conjugate system at high pH values; this process ultimately hinders the hydrolysis reaction by lowering the electrophilicity of the carbonyl groups[27]. Since the redox centre and the centre of electrophilic reactivity are separate in alloxazines, design strategies are available to decrease chemical reactivity, such as tuning the electrophilicity of alloxazines via different functional groups. We evaluated all of the screened alloxazines on the basis of their predicted equilibrium constant, K_{hyd}, for the reversible hydration of the carbonyl groups (Fig. 3b), with lower values of K_{hyd} corresponding to less electrophilic carbonyls. We found that the same electron-donating groups that contribute toward the desired reduction potential values also have a protecting effect against hydrolysis, as is the case with amides in general (that is, the hydrolysis rate of amides in basic medium has a linear dependence on K_{hyd})[28]. For instance, hydroxyl derivatives lower K_{hyd} by as much as two orders of magnitude, thereby shifting the equilibrium toward the redox-active 'de-hydrated' form.

Conclusions

By drawing inspiration from vitamin B_2, we introduced a family of organic molecules for RFB applications. The alloxazine redox centre exhibits sufficiently high electrochemical and chemical stability, and sufficiently low reduction potential, to be exploited as a negative electrolyte material in an alkaline RFB. Synthesis of a functionalized alloxazine redox-active centre was carried out via a very simple coupling chemistry utilizing only *o*-phenylenediamine derivatives, alloxan, acetic acid and boric acid, without employing high temperature or pressure. We paired alloxazine 7/8-carboxylic acid with ferri/ferrocyanide to demonstrate a high-performance alloxazine-powered RFB. The current efficiency exceeded 99.7% while its capacity retention over 400 charge–discharge cycles was shown to be ~95% cumulatively, or 99.98% per cycle. With a better understanding of the alloxazine system enabled by

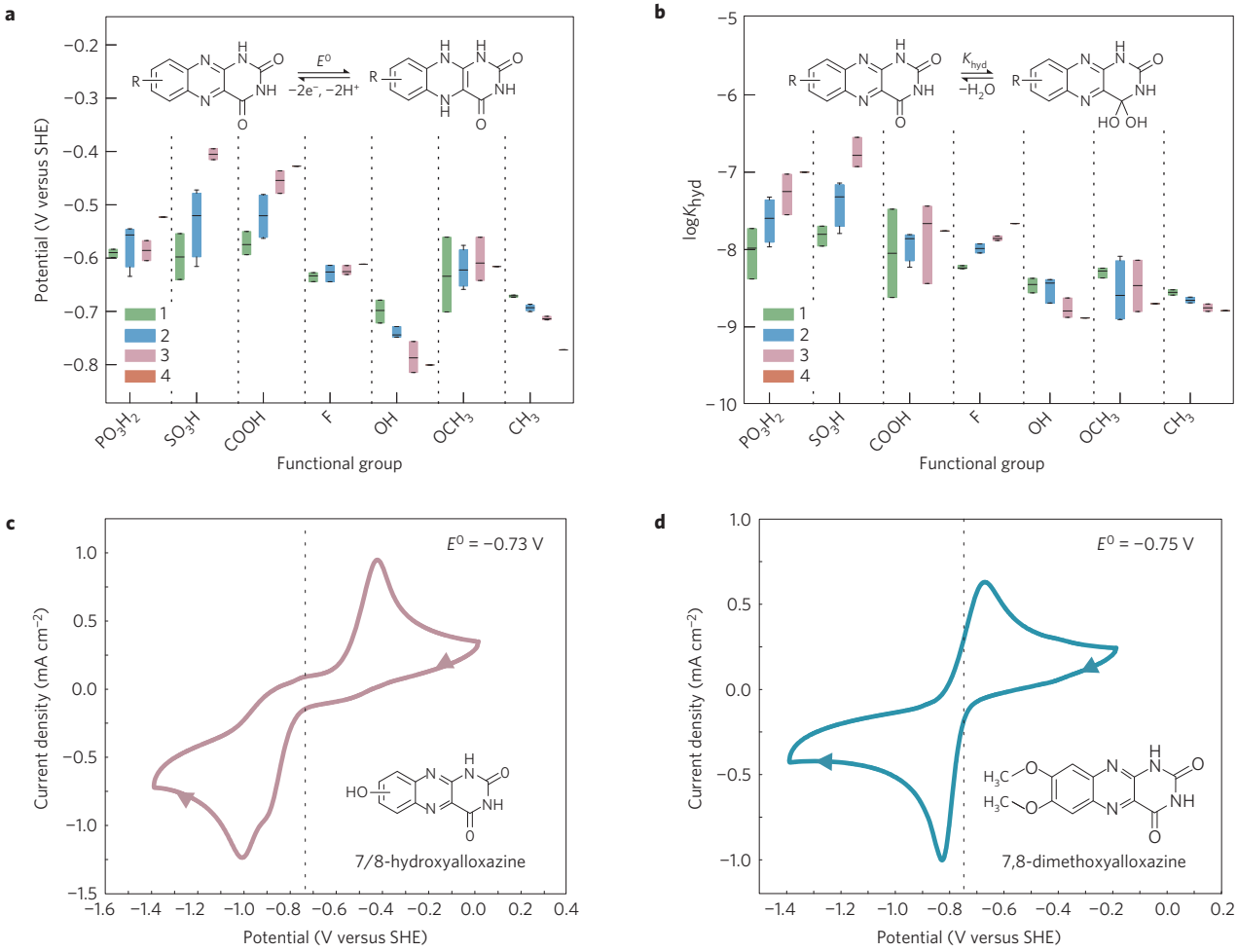

Figure 3 | Theoretical calculation and cyclic voltammetry of alloxazines. a, Predicted reduction potential at the B3LYP 6-311+G** CPCM level of theory for substituted alloxazines at pH 14.0 versus RHE as a function of number and type of substituent. **b**, Predicted logK_{hyd} at the B3LYP 6-311+G** CPCM level of theory for substituted alloxazines as a function of number and type of substituent. The bars represent the statistical distribution of predictions of all the possible substituted molecules with the given number of substituted sites. The bottom and top of the bar are the first and third quartiles, and the band inside the box is the median. The lines extending vertically from the boxes indicate the maximum and minimum of the range. **c**,**d**, Molecular structures and cyclic voltammogram of 1 mM 7/8-hydroxyalloxazine and 7,8-dimethoxyalloxazine, respectively, scanned at 100 mV s^{-1} on a glassy carbon electrode.

theoretical modelling, we have designed and characterized another two alloxazine-derived molecules promising almost 10% further increase in battery voltage. The introduction of aza-aromatic redox-active species opens up a new direction in designing organic electrolytes and delivers a promising pathway to accelerate the development of aqueous organic RFBs.

Methods

Chemical synthesis and characterization. 3,4-diaminophenol was purchased from Aurum Pharmatech and used as received. All other chemicals were purchased from Sigma-Aldrich and used as received. Alloxazines were prepared following previously reported methods[16–18]. In general, *o*-phenylenediamine (5 mmol) was added to 45 ml acetic acid followed by alloxan (5.5 mmol) and boric acid (5.5 mmol). The reaction mixture was stirred at room temperature and atmospheric pressure under nitrogen. The reaction times for various alloxazine derivatives are summarized in Table 2. After reaction, the product was collected by vacuum filtration, washed with acetic acid, water, and diethyl ether, and air-dried overnight. The products were analysed by ^{1}H NMR and used for chemical and electrochemical measurement without further purification. ^{1}H NMR spectra were recorded using Varian INOVA 500 (500 MHz) NMR spectrometers at 23 °C. Proton chemical shifts are expressed in parts per million (ppm, δ scale) and are referenced to residual protium in the NMR solvent (D_2O, δ 4.80 ppm and $(CD_3)_2SO$, δ 2.50 ppm). The isomeric ratio between major and minor products during the preparation of ACA and 7/8-hydroxyalloxazine was estimated on the basis of their peak integration ratio (highlighted in Supplementary Figs 2 and 10).

Stability test by ^{1}H NMR. In a nitrogen-filled glove bag, a sample of ACA (0.5 M) was dissolved in a solution of 40 wt% KOD in D_2O (used as received from Sigma-Aldrich), which was then adjusted to pH 14 with the appropriate amount of D_2O. The sample was sealed inside a J. Young tube and analysed by ^{1}H NMR. Analyses of the same sample were performed after 14, 21, 28 and 42 days. Between analyses, the J. Young tube was returned to the glove bag where it was kept in the dark. The proportion of ACA that had decomposed was determined by integrating the peaks at 6.48 ppm and comparing this area with the area of the peaks at 6.60 ppm and 6.86 ppm, which come from the starting material. From this data, the rate constant of ACA decomposition was calculated assuming first-order kinetics (Supplementary Fig. 4).

Solubility measurement by ultraviolet–visible spectroscopy. A saturated solution of ACA was prepared by addition of ACA to a pH 14 solution until a precipitate formed. KOH was added if necessary to maintain the solution pH. Aliquots of the supernatant were diluted with a pH 14 KOH solution and its absorbance was measured using ultraviolet–visible spectrophotometry (Ocean Optics FLAME-S-UV-VIS; cuvettes are made out of polystyrene with a path length of 1 cm). Readings were interpolated on the basis of a standard calibration curve prepared by measuring the absorbance of known concentrations of ACA (Supplementary Fig. 13).

Electrochemical analysis. Three-electrode cyclic voltammetry tests were performed using a glassy carbon working electrode, a Ag/AgCl reference electrode (pre-soaked in 3 M NaCl solution) and a platinum counter electrode. For the full cell measurements, cell hardware from Fuel Cell Tech. was used to assemble a zero-gap flow cell configuration, similar to previous reports[29]. POCO graphite flow plates with serpentine flow fields were used for both sides.

Table 3 | Theoretical calculation and substitution patterns of alloxazines.

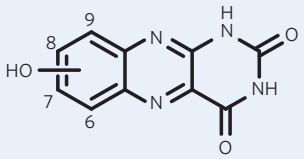

Hydroxylated alloxazines

No.	Position (-OH)				B3LYP 6-311+G** CPCM	
	6	7	8	9	E^{o} (V)	logK_{hyd}
1 substituent						
1	H	H	H	-OH	−0.69	−8.4
2	H	H	-OH	H	−0.72	−8.7
3	H	-OH	H	H	−0.68	−8.5
4	-OH	H	H	H	−0.77	−8.3
2 substituents						
5	-OH	-OH	H	H	−0.75	−8.4
6	-OH	H	-OH	H	−0.71	−8.6
7	-OH	H	H	-OH	−0.77	−8.2
8	H	-OH	-OH	H	−0.76	−9.3
9	H	-OH	H	-OH	−0.68	−8.4
10	H	H	-OH	-OH	−0.73	−8.7
3 substituents						
11	-OH	-OH	-OH	H	−0.81	−8.9
12	-OH	-OH	H	-OH	−0.74	−8.3
13	-OH	H	-OH	-OH	−0.82	−8.7
14	H	-OH	-OH	-OH	−0.74	−8.9
4 substituents						
15	-OH	-OH	-OH	-OH	−0.80	−8.9

Predicted standard reduction potential (E^{o}) and logarithmic hydration equilibrium constant (logK_{hyd}) for alloxazines with hydroxyl functional group(s).

Electrodes of 5 cm^2 geometric surface area were comprised of a stack of two or three sheets of Sigracet SGL 10AA porous carbon paper, which had been pretreated by baking in air at 400 °C for 24 h. A sheet of Nafion 212 membrane, pretreated in deionized water overnight, served as the ion-selective membrane. The rest of the space between the plates was gasketed by either Kalrez or Teflon sheets. The electrolytes were fed into the cell through PFA tubing, at a rate of 60 ml min^{-1} controlled by Cole-Parmer Masterflex L/S peristaltic pumps. All electrochemical tests were performed using a Gamry Reference 3000 potentiostat.

Rotating-disc electrode (RDE) measurement. RDE experiments were conducted using a BASi RDE (RDE-2) instrument equipped with a glassy carbon working electrode, a Ag/AgCl reference electrode (pre-soaked in 3 M NaCl solution) and a platinum counter electrode. The electrode was rotated at a specific speed while the voltage was linearly swept from −0.70 to −1.20 V versus Ag/AgCl. The reduction rate constant of ACA was calculated from the Tafel equation using the following parameters: $n = 2$; Faraday's constant $F = 96{,}485$ C mol^{-1}; electrode area $A = 0.0707$ cm^2, ACA concentration $C = 2 \times 10^{-6}$ mol cm^{-3}; kinematic viscosity $\nu = 0.01$ cm^2 s^{-1} (Supplementary Fig. 3). The experiment was performed three times.

Electrolyte preparation. For SOC, polarization and 400-cycle charge–discharge studies, the positive electrolyte was prepared by dissolving potassium ferrocyanide (1.9 g, 4.5 mmol) and potassium ferricyanide (0.15 g, 0.46 mmol) in 1 M KOH solution (11.25 ml) to afford 0.4 M electron concentration and 2.7 M K^+ ion solution (11 Ah l^{-1} charge density). The negative electrolyte was prepared by dissolving ACA (0.39 g, 1.5 mmol) in 2.5 M KOH solution (adjusted to final volume of 3 ml) to afford 1 M electron concentration and 2 M K^+ ion solution (27 Ah l^{-1} charge density). For the high-concentration ACA cycling experiment, the positive electrolyte was prepared by dissolving potassium ferrocyanide (3.8 g, 9 mmol) and potassium ferricyanide (0.3 g, 0.91 mmol) in 1 M KOH solution (22.5 ml) to afford a 0.4 M electron concentration and a 2.7 M K^+ ion solution (11 Ah l^{-1} charge density). The negative electrolyte was prepared by dissolving ACA (0.78 g, 3 mmol) in 4 M KOH solution (adjusted to final volume of 3 ml) to afford a 2 M electron concentration and 4 M K^+ ion solution (54 Ah l^{-1} charge density).

Computational studies. We have analysed all of the possible substitutions for each functional group on all of the possible sites of the alloxazine core. The functional groups assessed are carboxylic acid, fluoro, hydroxyl, methoxy, methyl, phosphonic acid and sulfonic acid. Substitution on the alloxazine amide nitrogens was not considered as they destabilize alloxazines under alkaline conditions. A total of 105 backbones were analysed. Initial conformations were generated that used a random-distance matrix approach at the mmff94 level of theory. Geometries were further refined using density functional theory (DFT) and single-point calculations were performed using larger basis sets and solvent corrections. The following methods were tested for obtaining equilibrium geometries and total energies: PM7, PM7 + implicit COSMO solvation, PBE/6-31G*, B3LYP/6-31G*. In addition, single-point calculations were performed at both B3LYP/6-311+G(d,p) and B3LYP/6-311+G(d,p) combined with CPCM implicit solvation. Their relative performance is compared in the Supplementary Information. For both target properties we obtained the smallest error using B3LYP/6-311+G(d,p) CPCM. Reduction potentials were predicted from the energy difference between the reduced and oxidized forms of alloxazines, assuming a two-electron two-proton process. Before conducting predictions, we assessed the performance of various quantum chemical methods to calculate the two-proton two-electron redox potential of alloxazine and isoalloxazine rings at pH = 7.4 using a calibration scheme analogous to the one reported for quinones. The calibration data set was composed of 23 experimentally reported molecules, with $E^{0}_{pH=7}$ ranging between −380 meV and −80 meV versus RHE[30]. Our results suggest that quick semiempirical methods and gas-phase DFT calculations afford results with mean errors around 20 meV. DFT calculations in implicit solvent with a larger basis set reduce the average error to under 10 meV. The performance of various methods is reported in Supplementary Table 2. We then corrected E^{0} values to pH = 14.0. Pourbaix diagrams were estimated combining experimental and predicted pK_a values (pK_a^{ox} = 8.3, 11.4; pK_a^{red} = 6.7, 10.0). The shift from pH = 7.4 to pH = 14.0 for alloxazines is thus estimated at −320 meV. To calculate hydration equilibrium, we used an experimental data set from the literature including aldehydes, ketones, esters and amides and mapped theoretical reaction energies at 0 K to experimentally determined hydration equilibrium constants in water[31]. The calibration data set was composed of 41 experimentally reported molecules, with logK_{hyd} ranging between −15 and 5. DFT calculations in implicit solvent result in mean errors close to 1 log unit. The performance of various methods is reported in Supplementary Table 2.

Received 4 April 2016; accepted 13 June 2016; published 18 July 2016

References

1. Dunn, B., Kamath, H. & Tarascon, J.-M. Electrical energy storage for the grid: a battery of choices. *Science* **334**, 928–935 (2011).
2. Nguyen, T. & Savinell, R. F. Flow batteries. *Electrochem. Soc. Interface* **19**, 54–56 (2010).
3. Yang, Z. *et al.* Electrochemical energy storage for green grid. *Chem. Rev.* **111**, 3577–3613 (2011).
4. Biello, D. Solar wars. *Sci. Am.* **311**, 66–71 (2014).
5. Skyllas-Kazacos, M., Chakrabarti, M. H., Hajimolana, S. A., Mjalli, F. S. & Saleem, M. Progress in flow battery research and development. *J. Electrochem. Soc.* **158**, R55–R79 (2011).
6. Weber, A. Z. *et al.* Redox flow batteries: a review. *J. Appl. Electrochem.* **41**, 1137–1164 (2011).
7. Perry, M. L. & Weber, A. Z. Advanced redox-flow batteries: a perspective. *J. Electrochem. Soc.* **163**, A5064–A5067 (2016).
8. Huskinson, B. *et al.* A metal-free organic-inorganic aqueous flow battery. *Nature* **505**, 195–198 (2014).
9. Huskinson, B., Marshak, M. P., Gerhardt, M. R. & Aziz, M. J. Cycling of a quinone-bromide flow battery for large-scale electrochemical energy storage. *ECS Trans.* **61**, 27–30 (2014).
10. Lin, K. *et al.* Alkaline quinone flow battery. *Science* **349**, 1529–1532 (2015).
11. Janoschka, T. *et al.* An aqueous, polymer-based redox-flow battery using non-corrosive, safe, and low-cost materials. *Nature* **527**, 78–81 (2015).
12. Schubert, U. S. *et al.* Polymer/zinc hybrid-flow battery using block copolymer micelles featuring a TEMPO corona as catholyte. *Polym. Chem.* **28**, 2238–2243 (2016).
13. Liu, T., Wei, X., Nie, Z., Sprenkle, V. & Wang, W. A total organic aqueous redox flow battery employing a low cost and sustainable methyl viologen anolyte and 4-HO-TEMPO catholyte. *Adv. Energy Mater.* **6**, 1501449 (2015).
14. Milstein, J. D., Liang, S., Liou, C., Badel, A. F. & Brushett, F. R. Voltammetry study of quinoxaline in aqueous electrolytes. *Electrochim. Acta* **180**, 695–704 (2015).
15. Brushett, F., Jansen, A. N., Vaughey, J. T. & Milshtein, J. D. Materials for use with aqueous redox flow batteries and related methods and systems. International Patent Application WO 2015/126907.

16. Chen, S., Hossain, M. S. & Foss, F. W. Organocatalytic dakin oxidation by nucleophilic flavin catalysts. *Org. Lett.* **14**, 2806–2809 (2012).
17. de Gonzalo, G., Smit, C., Jin, J., Minnaard, A. J. & Fraaije, M. W. Turning a riboflavin-binding protein into a self-sufficient monooxygenase by cofactor redesign. *Chem. Commun.* **47**, 11050–11052 (2011).
18. Lindén, A. A., Johansson, M., Hermanns, N. & Bäckvall, J.-E. Efficient and selective sulfoxidation by hydrogen peroxide, using a recyclable flavin-[BMIm]PF6 catalytic system. *J. Org. Chem.* **71**, 3849–3853 (2006).
19. Hasford, J. J. & Rizzo, C. J. Linear free energy substituent effect on flavin redox chemistry. *J. Am. Chem. Soc.* **120**, 2251–2255 (1998).
20. Müller, F. in *Radicals in Biochemistry* (eds Boschke, F. L. *et al.*) 71–107 (Springer, 1983).
21. Hong, J. *et al.* Biologically inspired pteridine redox centres for rechargeable batteries. *Nature Commun.* **5**, 5335 (2014).
22. Er, S., Suh, C., Marshak, M. P. & Aspuru-Guzik, A. Computational design of molecules for an all-quinone redox flow battery. *Chem. Sci.* **6**, 885–893 (2015).
23. Koziol, J. & Metzler, D. E. Formation and possible structure of covalent hydrates of alloxazines. *Z. Naturforsch. B* **27**, 1027–1029 (2014).
24. Surrey, A. R. & Nachod, F. C. Alkaline hydrolysis of riboflavin. *J. Am. Chem. Soc.* **73**, 2336–2338 (1951).
25. Ahmad, I., Rapson, H. D. C., Heelis, P. F. & Phillips, G. O. Alkaline hydrolysis of 7,8-dimethyl-10-(formylmethyl)isoalloxazine. A kinetic study. *J. Org. Chem.* **45**, 731–733 (1980).
26. Prukała, D. *et al.* Acid–base equilibriums of lumichrome and its 1-methyl, 3-methyl, and 1,3-dimethyl derivatives. *J. Phys. Chem. A* **116**, 7474–7490 (2012).
27. Koziol, J., Tyrakowska, B. & Müller, F. The structure of covalent hydrates of alloxazines. A reinvestigation. *Helv. Chim. Acta* **64**, 1812–1817 (1981).
28. O'Connor, C. Acidic and basic amide hydrolysis. *Q. Rev. Chem. Soc.* **24**, 553–564 (1970).
29. Liu, Q. H. *et al.* High performance vanadium redox flow batteries with optimized electrode configuration and membrane selection. *J. Electrochem. Soc.* **159**, A1246–A1252 (2012).
30. Li, X.-L. & Fu, Y. Theoretical study of reduction potentials of substituted flavins. *J. Mol. Struct. THEOCHEM* **856**, 112–118 (2008).
31. Gómez-Bombarelli, R., González-Pérez, M., Pérez-Prior, M. T., Calle, E. & Casado, J. Computational calculation of equilibrium constants: addition to carbonyl compounds. *J. Phys. Chem. A* **113**, 11423–11428 (2009).

Acknowledgements

This work was funded by the US DOE ARPA-E award no. DE-AR0000348, NSF no. NSF-CBET-1509041, the Massachusetts Clean Energy Technology Center, and the Harvard John A. Paulson School of Engineering and Applied Sciences. We thank C. Qian for designing the Fig. 1d scheme. We appreciate support from the Odyssey Cluster and Research Computing of Harvard University's Faculty of Arts and Sciences.

Author contributions

K.L., R.G.G. and M.J.A. formulated the project. K.L. and L.T. synthesized the compounds. K.L., E.S.B. and L.T. collected and analysed the NMR data. K.L., Q.C., E.S.B. and A.V. collected and analysed the electrochemical data. K.L. and A.V. measured solubility. R.G.-B. and A.A.-G. performed theoretical analysis. K.L., R.G.G. and M.J.A. wrote the paper, and all authors contributed to revising the paper.

Additional information

Supplementary information is available online. Reprints and permissions information is available online at www.nature.com/reprints. Correspondence and requests for materials should be addressed to M.J.A. or R.G.G.

Competing interests

The authors declare no competing financial interests.

A redox flow battery with an alloxazine-based organic electrolyte

Kaixiang Lin[1], Rafael Gómez-Bombarelli[1], Eugene S. Beh[1,2], Liuchuan Tong[1], Qing Chen[2], Alvaro Valle[3], Alán Aspuru-Guzik[1], Roy G. Gordon[1,2*], Michael J. Aziz[2*]

[1]Department of Chemistry and Chemical Biology, Harvard University, 12 Oxford Street, Cambridge, Massachusetts 02138, USA.

[2]Harvard John A. Paulson School of Engineering and Applied Sciences, 29 Oxford Street, Cambridge, Massachusetts 02138, USA.

[3]Harvard College, Cambridge, Massachusetts 02138, USA

[*]Correspondence to: RGG (gordon@chemistry.harvard.edu) and MJA (aziz@seas.harvard.edu)

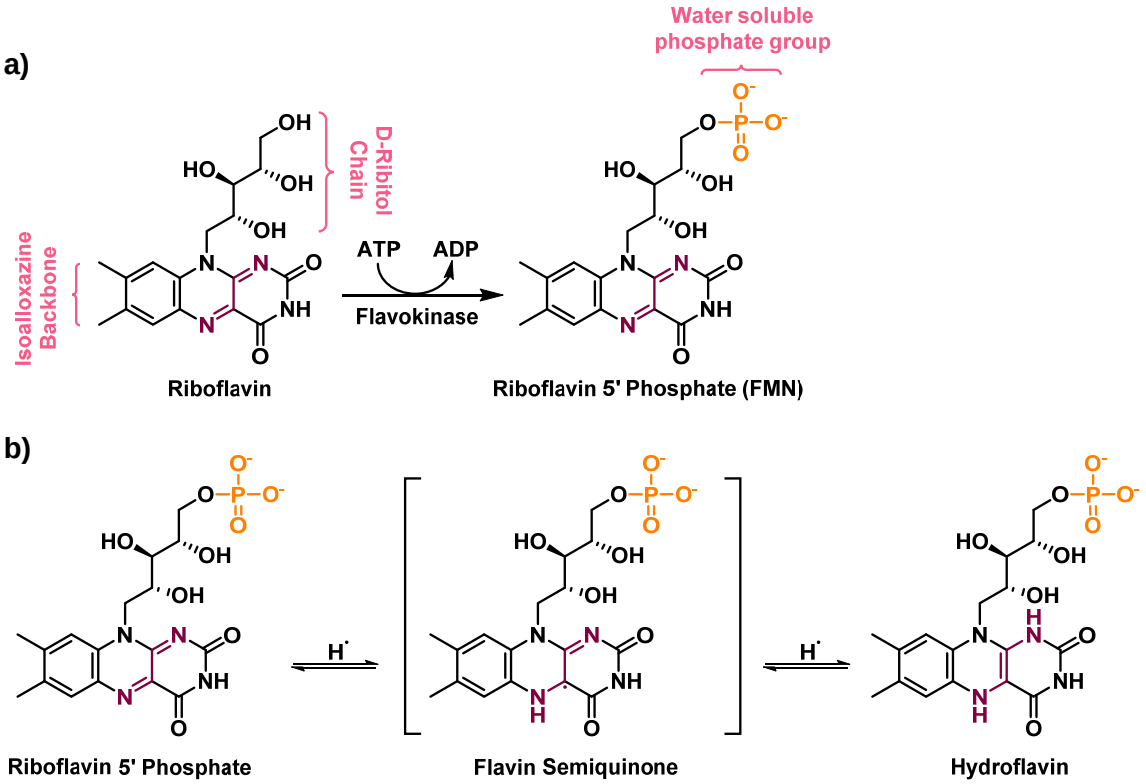

Supplementary Figure 1. (a) Biosynthesis of riboflavin 5' phosphate (FMN) from riboflavin (vitamin B_2). **(b)** Stepwise reduction of FMN into hydroflavin.[18]

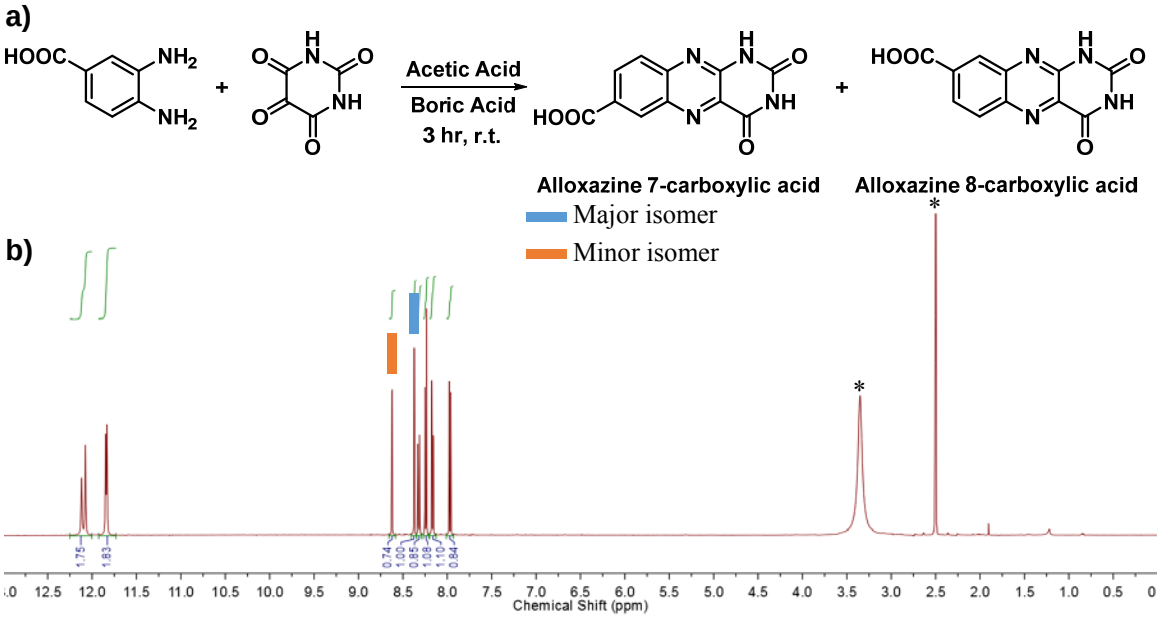

Supplementary Figure 2. (a) Synthetic scheme of alloxazine 7/8-carboxylic acid. **(b)** ^{1}H NMR (500 MHz, DMSO-d_6) spectrum of alloxazine 7/8-carboxylic acid. Major isomer: δ 12.02 (s, 1H), 11.79 (s, 1H), 8.29 (d, J = 1.9 Hz, 1H), 8.18 (d, J = 8.8 Hz, 1H), 8.09 (dd, J = 1.9, 8.8 Hz, 1H). Minor isomer: δ 12.06 (s, 1H), 11.80 (s, 1H), 8.55 (d, J = 2.0 Hz, 1H), 8.25 (dd, J = 2.0, 8.8 Hz, 1H), 7.90 (d, J = 8.8 Hz, 1H). Solvent peaks are labeled with asterisks. Final yield: 95%.

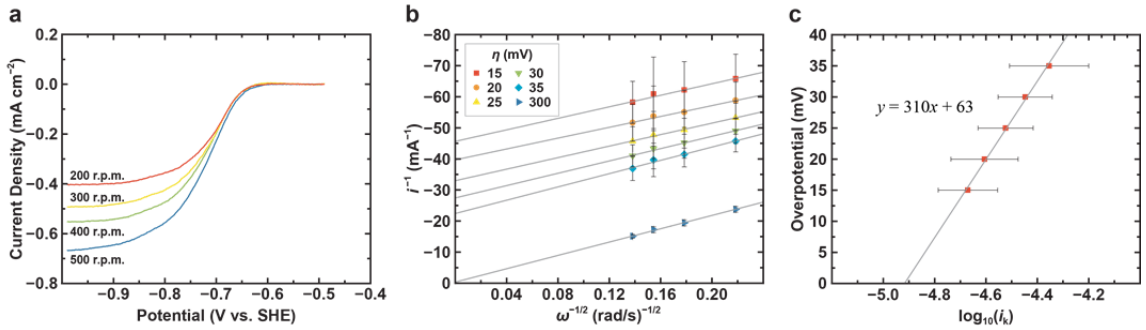

Supplementary Figure 3. (a) Plot of potential versus current density at different rotation rates of the RDE. The solution is 2 mM ACA in 1 M aqueous KOH, using a rotating disk electrode (RDE) of glassy carbon. Rotation rates are indicated. **(b)** Koutecký-Levich plot (i^{-1} versus $\omega^{-1/2}$) of 2 mM ACA in 1 M aqueous KOH. The current response, i^{-1}, is shown for six different ACA reduction overpotentials η. (**c**) Fit of RDE experimental data to the Tafel equation constructed using the current response in the absence of mass transport limitations at low ACA reduction potentials; i_k is the current extrapolated from the zero-intercept of the fitted lines in (b) (i.e. at infinite rotation rate). The line of best fit has the equation $y = 310x + 63$, from which $\alpha = 0.47(4)$ and $k_0 = 1.2(2) \times 10^{-5}$ cm s^{-1} were calculated. Data are averaged over three runs; the numbers reported in parentheses indicate the standard deviation in the last reported digit.

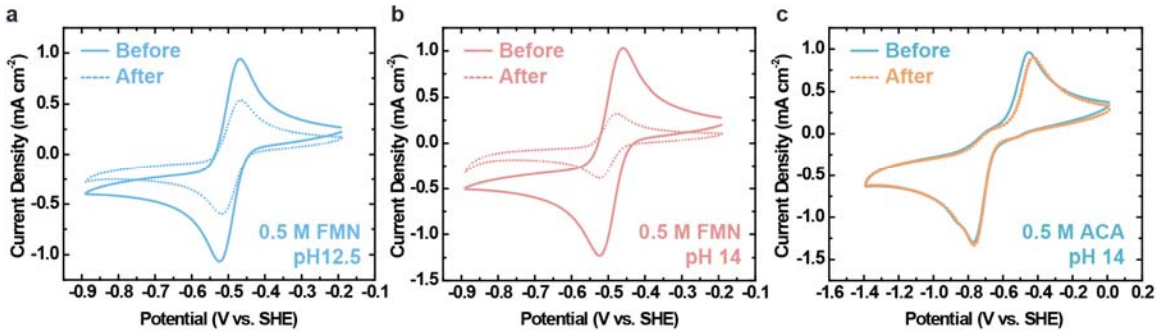

Supplementary Figure 4. (a) Cyclic voltammogram of 1/1000th dilution of riboflavin 5' phosphate (FMN) at pH 12.5 before (solid line) and after (dotted line) 14 days, scanned at 100 mV/s on a glassy carbon electrode. **(b)** and **(c)** Cyclic voltammogram of 1/1000th dilution of riboflavin 5' phosphate (FMN) and alloxazine 7/8-carboxylic acid (ACA), respectively, at pH 14 before (solid line) and after (dotted line) 14 days, scanned at 100 mV/s on a glassy carbon electrode.

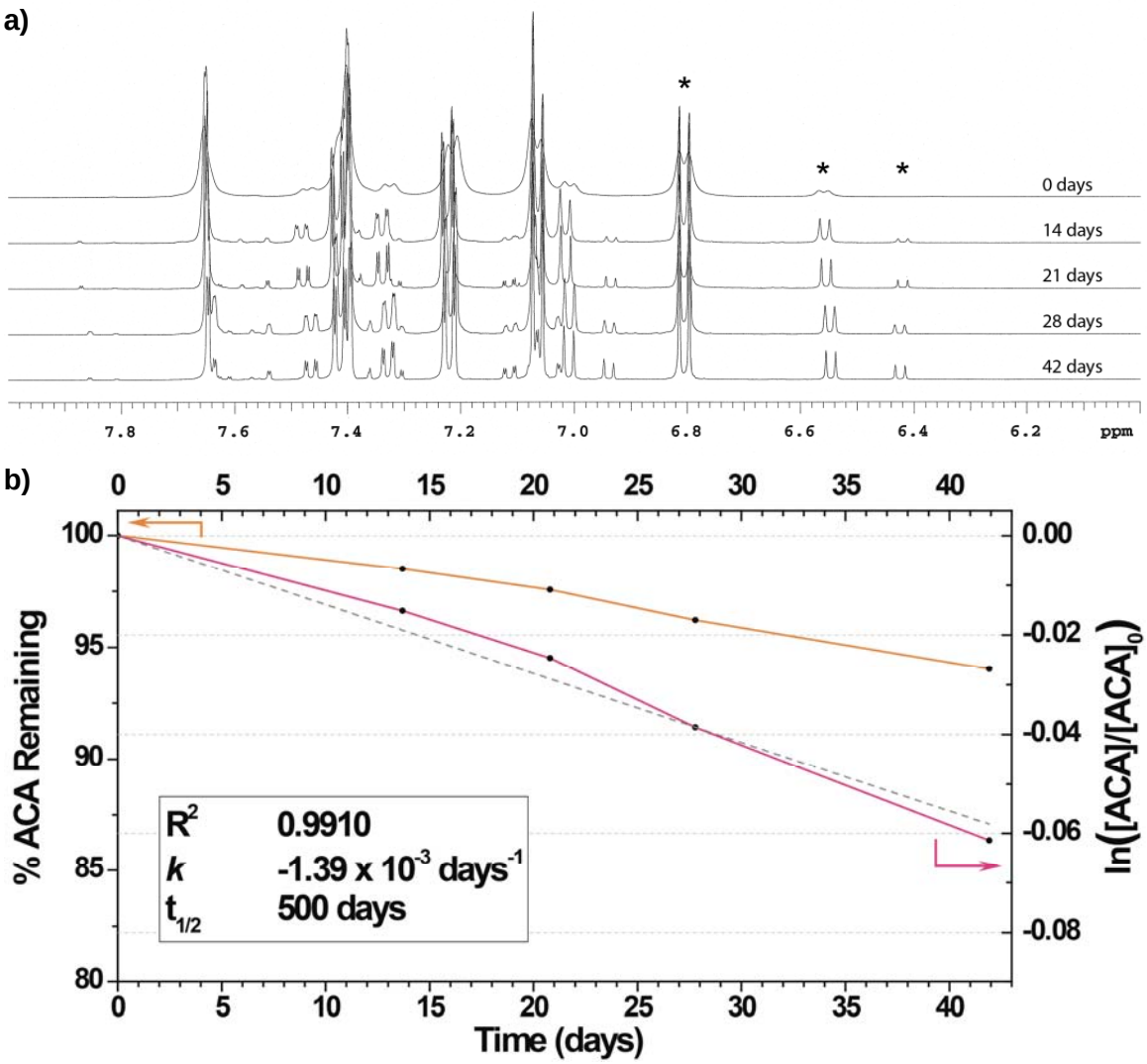

Supplementary Figure 5. ^{1}H NMR study of ACA stability in solution. **(a)** ^{1}H NMR spectra of a sample of 0.5 M ACA at pH 14 after various time points. The proportion of ACA that had decomposed was determined by comparing the area of the doublet that emerges at 6.43 ppm to the sum of the areas of the doublets at 6.55 ppm and 6.81 ppm, which come from the starting material. The peaks of interest are marked with a star. **(b)** Graphical depiction of the percentage of ACA remaining in the sample as a function of time (orange trace, left axis), as well as the same data replotted assuming first-order kinetics (pink trace, right axis). The gray dashed line represents the least-squares linear fit to the data in the pink trace.

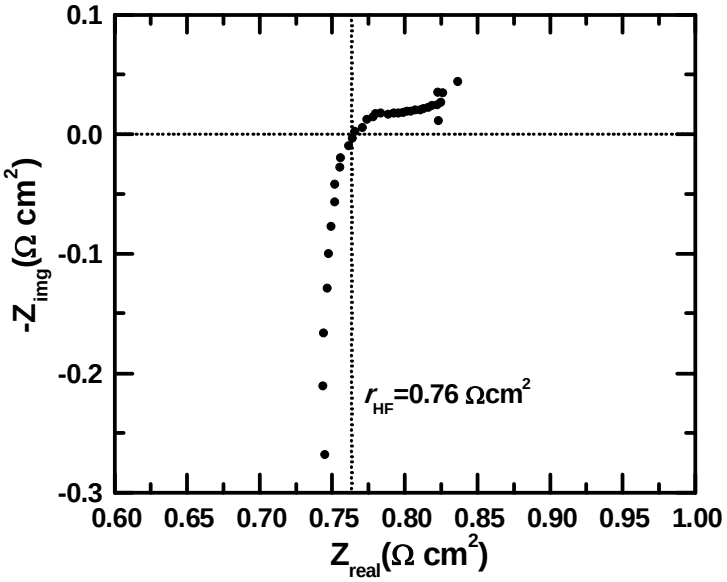

Supplementary Figure 6. Electrochemical impedance spectroscopy (EIS) of the ACA-ferrocyanide cell discussed in **Fig. 3a and 3b**. The EIS data were captured at 50% SOC. A high-frequency ASR (r_{HF}) was taken at ~80 kHz to be 0.76 Ω cm^2. This comprises the membrane ionic resistance, the electrode electronic resistances, and the contact resistances, but not the electrolyte resistances. As the sum of the cell contact resistance and the electrode electronic resistance was previously measured in a dry-cell (a setup identical to the flow cell, but without the membrane and the flowing electrolyte) to be ~0.02 Ωcm^2, the membrane resistance, by subtraction, is thus ~0.74 Ωcm^2.

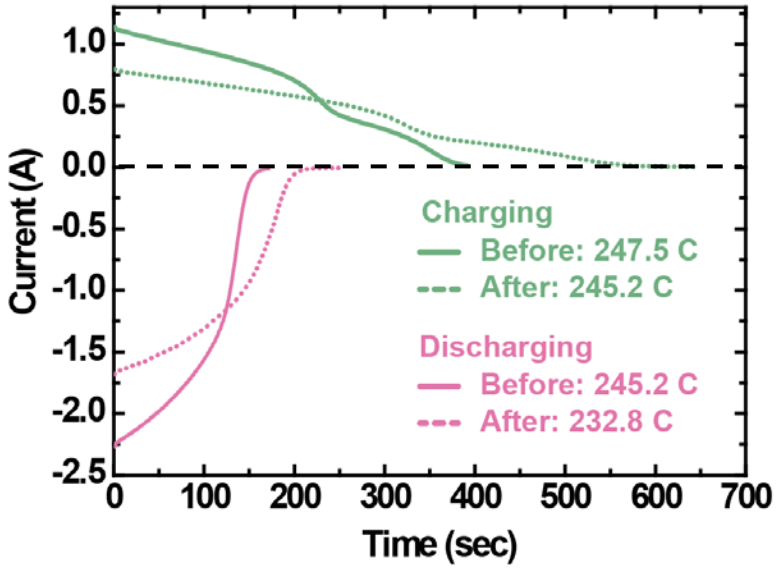

Supplementary Figure 7. Chronoamperometric (constant voltage) charging and discharging of ACA before (solid line) and after (dotted line) the 400 cyclic charge-discharge study. Black dashed line indicates zero current. Integration of the curves gives a 95% discharge capacity retention after 400 cycles.

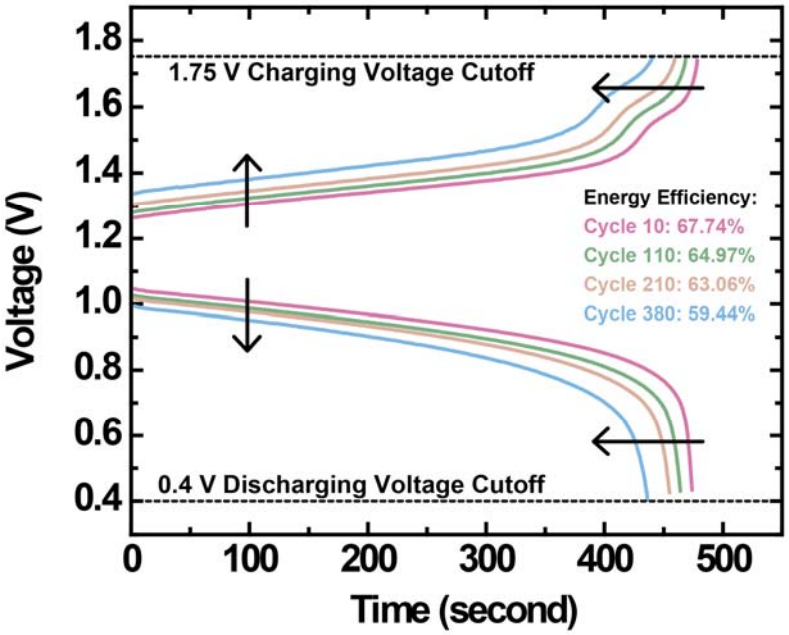

Supplementary Figure 8. Charging and discharge profiles of ACA at cycle no. 10, 110, 210 and 380 in the 400-cycle charge-discharge study. Black dashed lines indicate the voltage cutoffs. Black arrows represent the shifting directions of the curves during the course of the cycling study.

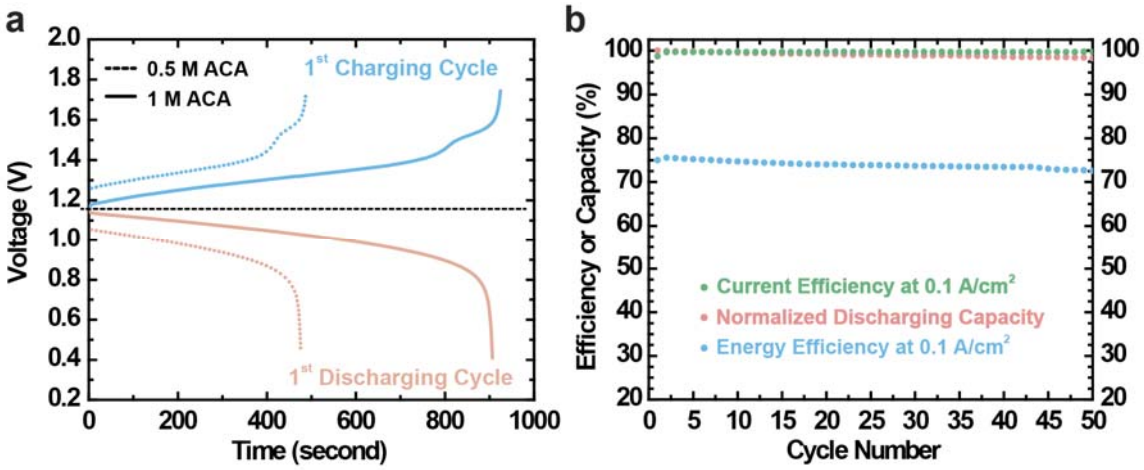

Supplementary Figure 9. (**a**) Representative voltage vs. time curves of the 1st charge-discharge cycle at 0.1 A/cm^2 for 0.5 M ACA (dotted line) and 1 M ACA (solid line) vs. 0.4 M ferrocyanide + 40 mM ferricyanide**.** (**b**) Capacity retention (97.5%), current efficiency (99.7%) and energy efficiency (74%) values measured over 50 charge-discharge cycles of the 1 M ACA negative electrolyte at 0.1 A/cm^2. Normalized discharging capacity is evaluated based on the capacity of the first discharge cycle.

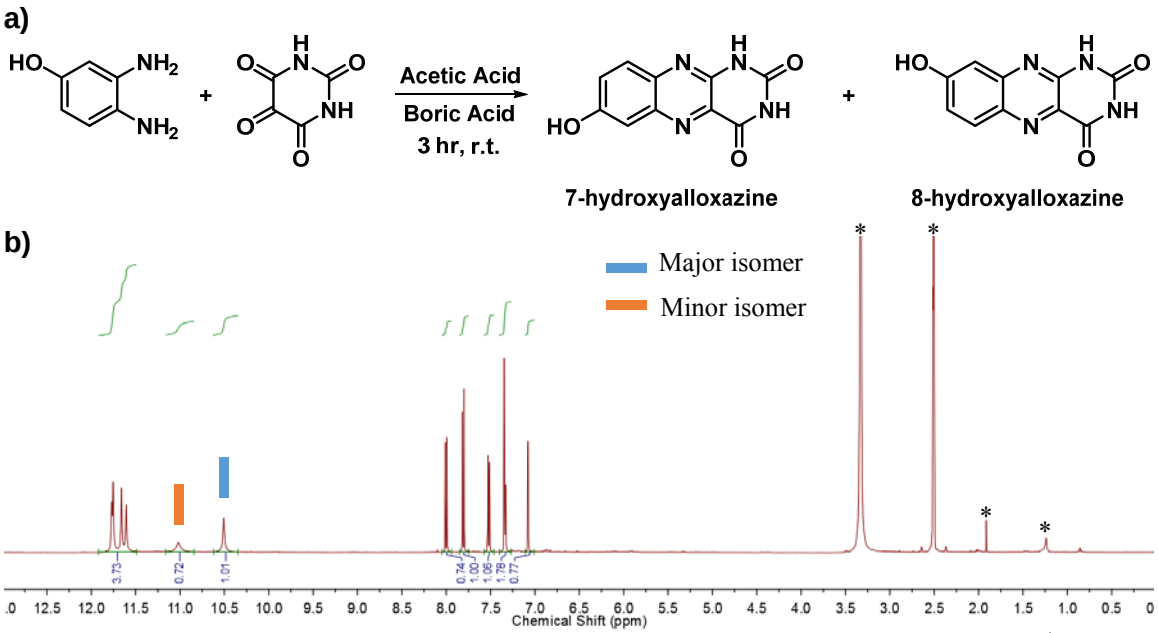

Supplementary Figure 10. (a) Synthetic scheme for 7/8-hydroxyalloxazine. **(b)** ^{1}H NMR (500 MHz, DMSO-d_6) spectrum of 7/8-hydroxyalloxazine. Major isomer: δ 12.02 (s, 1H), 11.79 (s, 1H), 8.29 (d, J = 1.9 Hz, 1H), 8.18 (d, J = 8.8 Hz, 1H), 8.09 (dd, J = 1.9, 8.8 Hz, 1H). Minor isomer: δ 12.06 (s, 1H), 11.80 (s, 1H), 8.55 (d, J = 2.0 Hz, 1H), 8.25 (dd, J = 2.0, 8.8 Hz, 1H), 7.90 (d, J = 8.8 Hz, 1H). Solvent peaks are labeled with asterisks. Final yield: 86%.

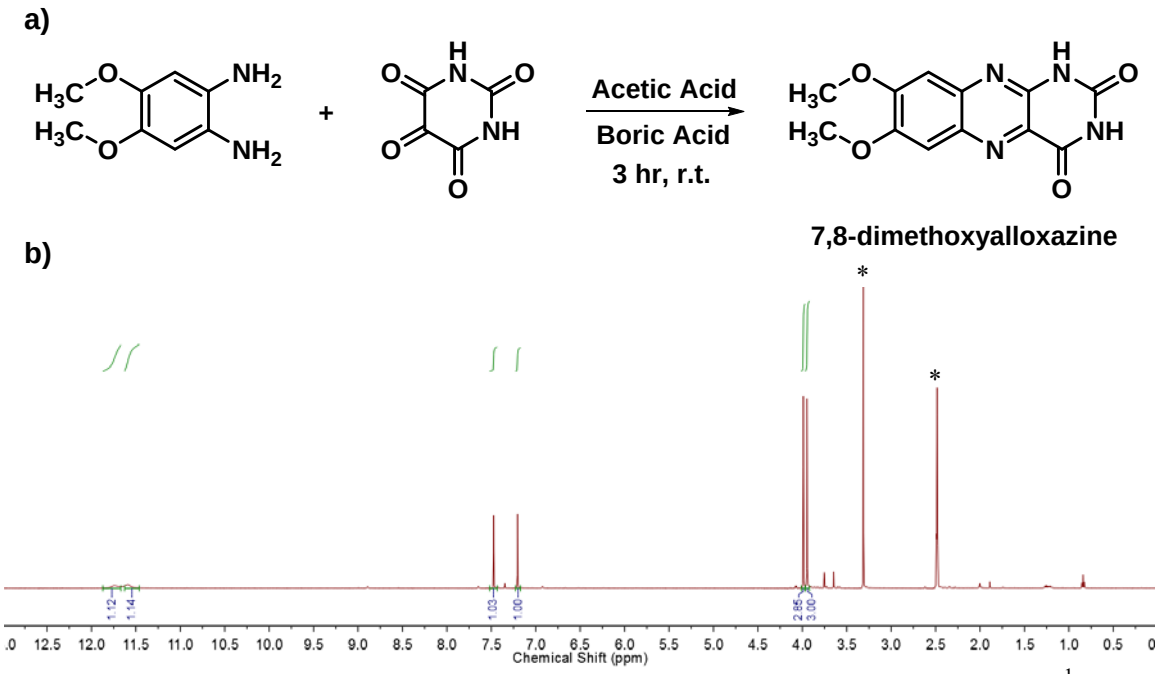

Supplementary Figure 11. (a) Synthetic scheme of 7,8-dimethoxyalloxazine. **(b)** ^{1}H NMR (500 MHz, DMSO-d_6) spectrum of 7,8-dimethoxyalloxazine δ 12.02 (s, 1H), 11.79 (s, 1H), 8.29 (d, J = 1.9 Hz, 1H), 8.18 (d, J = 8.8 Hz, 1H), 8.09 (dd, J = 1.9, 8.8 Hz, 1H). Solvent peaks are labeled with asterisks. Final yield: 94%.

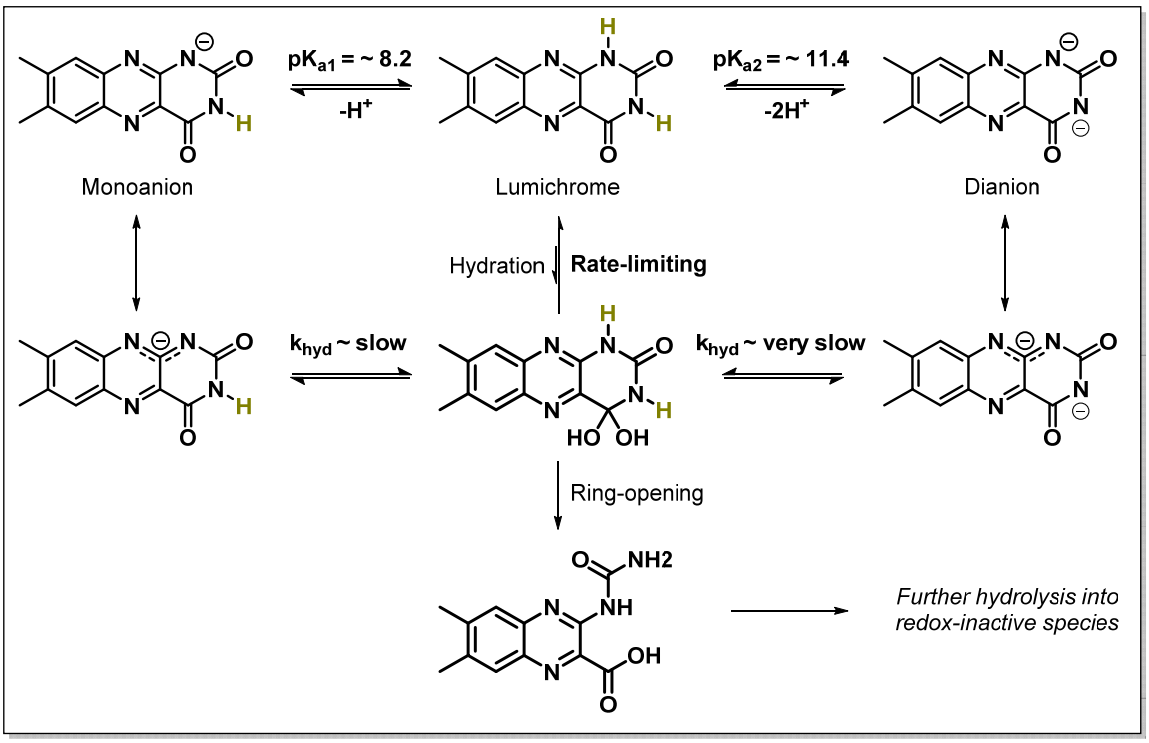

Supplementary Figure 12. Deprotonation, hydration and ring-opening reactions of lumichrome (7,8-dimethylalloxazine).[20]

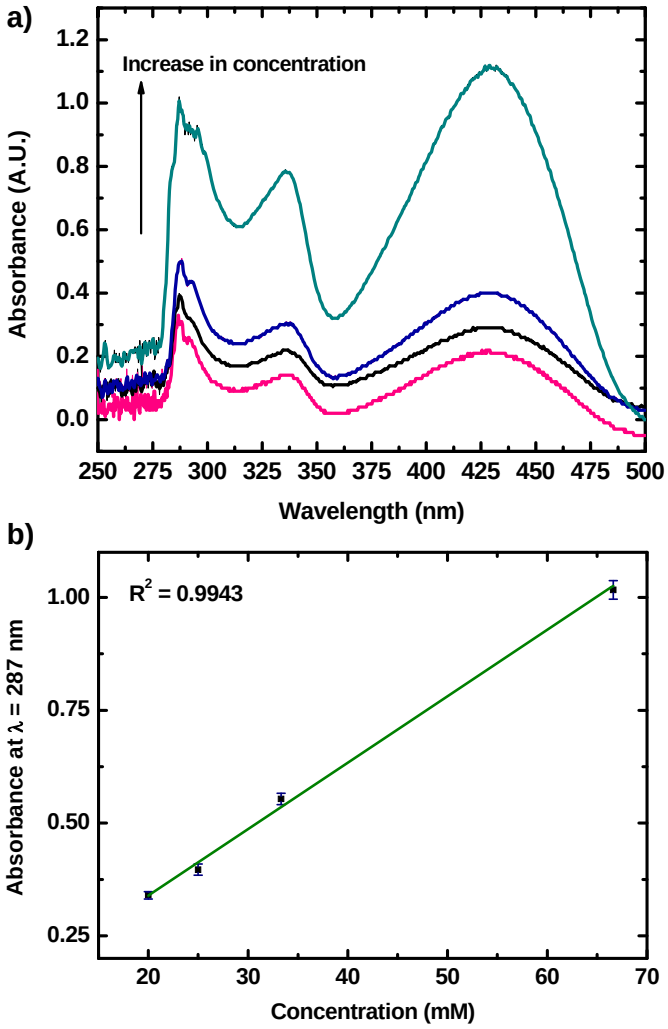

Supplementary Figure 13. (a) UV-Vis spectra of ACA at different concentration. **(b)** Standard calibration curve of ACA absorbance at $\lambda = 287$ nm vs. concentration. This calibration curve was interpolated to determine the concentration of ACA in diluted aliquots of a saturated solution, from which the saturation concentration of ACA was calculated.

Supplementary Table 1. Substitution patterns and predicted standard reduction potential (E^o) and logarithmic hydration equilibrium constant ($\log K_{hyd}$) for alloxazines.

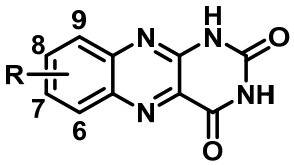

alloxazine derivatives

Position				B3LYP 6-311+G** CPCM											
6	7	8	9	E^o (V)	$\log K_{hyd}$	E^o (V)	$\log K_{hyd}$	E^o (V)	$\log K_{hyd}$	E^o (V)	$\log K_{hyd}$	E^o (V)	$\log K_{hyd}$	E^o (V)	$\log K_{hyd}$
1 substituent				R = $-PO_3H_2$		R = $-SO_3H$		R = -COOH		R = -F		R = $-OCH_3$		R = $-CH_3$	
H	H	H	R	-0.62	-9.4	-0.67	-7.7	-0.53	-6.1	-0.63	-8.1	-0.54	-8.3	-0.67	-8.5
H	H	R	H	-0.57	-8.0	-0.52	-7.9	-0.56	-7.9	-0.66	-8.2	-0.71	-8.2	-0.68	-8.6
H	R	H	H	-0.59	-7.2	-0.57	-7.7	-0.60	-8.2	-0.64	-8.3	-0.70	-8.6	-0.67	-8.6
R	H	H	H	-0.59	-7.9	-0.63	-8.1	-0.59	-10.0	-0.63	-8.2	-0.57	-8.3	-0.67	-8.5
2 substituents															
R	R	H	H	-0.52	-9.0	-0.47	-9.4	-0.56	-8.2	-0.63	-8.0	-0.61	-7.7	-0.68	-8.6
R	H	R	H	-0.64	-7.7	-0.54	-7.8	-0.49	-10.4	-0.64	-8.1	-0.63	-8.9	-0.70	-8.8
R	H	H	R	-0.63	-7.3	-0.63	-7.4	-0.45	-7.8	-0.61	-7.9	-0.49	-8.1	-0.69	-8.6
H	R	R	H	-0.55	-7.3	-0.50	-7.2	-0.57	-7.9	-0.65	-8.0	-0.76	-8.3	-0.70	-8.7
H	R	H	R	-0.56	-7.5	-0.62	-7.1	-0.48	-7.8	-0.61	-7.9	-0.58	-9.2	-0.69	-8.7
H	H	R	R	-0.55	-8.0	-0.47	-7.0	-0.56	-7.7	-0.62	7.9	-0.66	-8.9	-0.69	-8.6
3 substituents															
R	R	R	H	-0.60	-7.4	-0.41	-6.9	-0.44	-7.9	-0.63	-7.9	-0.64	-8.1	-0.71	-8.6
R	R	H	R	-0.61	-7.1	-0.40	-7.1	-0.43	-7.4	-0.59	-7.8	-0.51	-8.2	-0.70	-8.7
R	H	R	R	-0.57	-8.2	-0.38	-6.1	-0.47	-10.1	-0.62	-7.8	-0.58	-8.8	-0.71	-8.9
H	R	R	R	-0.56	-6.8	-0.43	-6.7	-0.51	-7.4	-0.63	-7.9	-0.64	-8.9	-0.72	-8.8
4 substituents															
R	R	R	R	-0.52	-9.7	-0.35	-6.3	-0.43	-7.8	-0.61	-7.7	-0.62	-8.7	-0.77	-8.8

Supplementary Table 2. Predicted error in standard reduction potential (E^0) values for (iso)alloxazine molecules at pH = 7.4 and in logarithmic hydration equilibrium constant ($logK_{hyd}$) values.

Method	E^0 (V)		$logK_{hyd}$	
	R^2	Mean Error (meV)	R^2	Mean Error (log units)
PM7	0.86	23	0.79	1.5
PM7 COSMO	0.90	24	0.88	1.3
PBE 6-31G*	0.90	24	0.88	1.2
B3LYP 6-31G*	0.87	27	0.89	1.1
B3LYP 6-311+G**	0.89	25	0.85	1.2
B3LYP 6-311+G** CPCM	0.97	8	0.90	1.0